

## Fragmentation of Bi clusters by multiply charged ions

A. Mika, P. Rouseau, A. Domaracka,<sup>\*</sup> and B. A. Huber<sup>†</sup>

*Normandie Univ, ENSICAEN, UNICAEN, CEA, CNRS, CIMAP, 14000 Caen, France*



(Received 3 October 2018; published 17 January 2019)

We report on collisions of multiply charged ions with free Bi nanoparticles in the gas phase. The nanoparticles contain up to 650 Bi atoms corresponding to a diameter of 3.5 nm. The stability limit of multiply charged Bi clusters has been investigated yielding appearance sizes for Bi clusters in charge states up to  $q = 6$ , which are in good agreement with predictions of the liquid drop model. This finding underlines the metallic character of the Bi particles. By coincidence measurements the correlation between the dominant fragments  $\text{Bi}^+$  and  $\text{Bi}_3^+$  and larger multiply charged residues has been determined. The comparison of the kinetic energies with  $Q$ -value calculations within the liquid drop model allowed identifying specific decay processes as two-body asymmetric fission or multifragmentation events. The higher kinetic energies of singly charged monomer ions compared to that of trimer ions are explained by a higher fissility of the decaying system. Correlation islands for small fragments indicate different decay mechanisms based on two-step processes where a third undetected fragment can be emitted in the first or the second step.

DOI: [10.1103/PhysRevA.99.012707](https://doi.org/10.1103/PhysRevA.99.012707)

### I. INTRODUCTION

Recently large metallic nanoparticles with diameters of several nm have become the object of intense research concerning their interaction with multiply charged ions. This is due to the fact that these nanoparticles are used as radio sensitizers in the treatment of cancer by the so-called nanoparticle-enhanced ion beam cancer therapy [1]. In general it was shown that when metallic nanoparticles are placed into tumor cells before irradiation with x rays or high-energy ions [2,3], the survival of tumorous cell cultures is strongly reduced. Thus, metallic nanoparticles of silver, gold, and platinum showed a reduction effect of up to 30%, which is explained by the production of secondary particles either in the form of an increased secondary electron yield or in the formation of radical species [4,5]. Hossain *et al.* [6] found that for 50 keV proton irradiation, bismuth nanoparticles showed a dose enhancement with respect to Au and platinum nanoparticles (for a given nanoparticle size, concentration, and location) of 1.25 and 1.29, respectively. Correspondingly, the Auger electron yield for bismuth nanoparticles is found to be 2 to 2.4 times higher than for the other two nanoparticles.

Furthermore, bismuth has many peculiar properties which make it unique among the metals. Thus, it shows the largest diamagnetism, has a very low thermal conductivity and a high electrical resistivity which is about 80 times larger than that of copper or silver. Among the heavy metals bismuth is a material with low toxicity and undergoes a phase transition when the size of the system decreases. For thin layers, Hoffman *et al.* [7] confirmed the longstanding theoretical prediction that quantum confinement should convert Bi from a semimetal to a semiconductor at a critical thickness of the order of 300 Å. For all these reasons bismuth is widely used in industry,

as well as in biological and medical sciences [8]. Recently bismuth nanoparticles have drawn great attention for application in biological sciences such as bioimaging, biosensing, biomolecular detection, and x-ray radiosensitizing.

Collision experiments with clusters of bismuth are very scarce. On the one hand, small  $\text{Bi}_n^+$  cations with sizes  $n = 3-8$  have been collided at 75 eV with HOPG surfaces, and the induced fragmentation processes have been analyzed by mass spectrometry, yielding dominantly small fragments of  $\text{Bi}^+$  to  $\text{Bi}_3^+$  [9]. On the other hand, an early collision experiment of electrons with small neutral Bi clusters has been reported [10]. When the initial distribution of Bi clusters contained only very small clusters, the appearance size of the dication was found to be as low as 5; this value increases when larger cluster sizes are irradiated. From these observations it was concluded that small Bi clusters are not metallic but rather do have the character of a semiconductor. Information on the structure of small  $\text{Bi}_n^+$  clusters ( $n = 4-14$ ) has been obtained by experimental studies based on ion mobility spectrometry and density functional theory calculations [11]. It is found that for  $n > 8$  the clusters adopt a prolate structure with highly directional bonds. These open structures are typical for clusters of semiconducting elements rather than resembling the compact structures typical for clusters of metallic elements. More recently, photoelectron spectroscopy of free Bi clusters containing tens to hundreds of atoms has been performed suggesting the metallic character of Bi clusters with sizes of a few nm [12].

Collisions with photons have been performed with various metallic clusters; in particular alkali clusters have been studied with the aim to analyze fragmentation and ionization processes, specifying direct ionization or collective optical excitations [13,14]. Furthermore, processes like symmetric and asymmetric fission have been discussed. The stability and fragmentation of sodium clusters have been studied in early experiments concerning collisions of various multiply charged ions in charge states between 2 and 28 with neutral

<sup>\*</sup>domaracka@ganil.fr

<sup>†</sup>huber@ganil.fr

sodium clusters containing typically 200 atoms [15,16]. It was shown that asymmetric fission dominates and that the observed appearance sizes vary with the internal energy of the system, i.e., the charge state of the projectile.

In the present contribution we will discuss collisions of multiply charged ions, in particular of  $\text{Ar}^{8+}$  ions at a kinetic energy of 120 keV with  $\text{Bi}_n^+$  clusters containing between  $\sim 15$  and  $\sim 300$  atoms, i.e., with typical cluster diameters of 2–3 nm with masses of up to 60 000 amu. We will discuss the dominant fragmentation pathways, their metallic behavior and the validity of the application of the liquid drop model.

## II. EXPERIMENTAL METHOD

The experiments were performed at the ARIBE facility at the GANIL laboratory in Caen, France. The ion beams are produced by means of an electron cyclotron resonance ion source (165 keV  $\text{Ar}^{11+}$ , 120 keV  $\text{Ar}^{8+}$ , 90 keV  $\text{O}^{6+}$ , and 45 keV  $\text{O}^{3+}$ ). The ion beams were pulsed: 1  $\mu\text{s}$  long bunches with a repetition rate of about 1 kHz. A detailed description of the experimental method is given in Ref. [17].

Bismuth clusters are produced by means of a magnetron discharge cluster source. This source is a combination of the magnetron sputtering device assisted by a magnetic field and a cylindrical gas aggregation chamber (a similar device is used by the group of von Issendorff *et al.* [18]). The cathode of the discharge is a metallic disk of dimensions of 0.25 inch in thickness and 2 inches in diameter (Lesker, purity of 99.99%). Bi is sputtered by energetic argon ions produced in a continuous plasma discharge. The assisting magnetic field which increases the discharge density is produced by a set of two concentric rings. The condensation chamber where cluster formation takes place has a double wall and can be cooled down to the temperature of liquid nitrogen. The aggregation length can be varied between 5 and 25 cm to produce different size distribution of clusters. For the present experiments the temperature was kept at  $-170^\circ\text{C}$  with a discharge power of around 20 W, an Ar buffer gas flow of 100 ml/min, and an aggregation length of 25 cm.

The produced  $\text{Bi}_n$  clusters are neutral or singly charged (positively or negatively) and can be separated from each other in a preparation chamber by electric fields. Only neutral clusters enter the interaction zone and cross the ion beam. Cationic products of the interaction (ionized clusters and cluster fragments) are extracted orthogonally by a pulsed electric field and pass a field-free drift region (1 m in length) in the time-of-flight mass spectrometer after which they are postaccelerated towards a conversion plate placed at a voltage of  $-19$  kV. The detection of secondary electrons is made by microchannel plates after deflection by Helmholtz coils. This Daly-type detector allows improving the detection for heavy products. Nevertheless, the detection efficiency is limited towards very large cluster sizes.

Neutral Bi clusters can also pass through the interaction zone and enter a deposition chamber, where they are deposited on  $\text{SiO}_2$  substrates or transmission electron microscopy (TEM) grids for further analysis of their size distributions by applying atomic force microscopy (AFM) or TEM techniques.

## III. EXPERIMENTAL RESULTS AND DISCUSSION

The size distribution of neutral bismuth clusters has been estimated by the analysis of TEM images of deposited clusters. Many small-size clusters are observed with a measured average cluster diameter of the order of 2 nm [see Fig. 1(a)]. This corresponds to clusters containing 120 atoms; clusters with diameters between 1.5 and 3.5 nm contain  $\sim 40$  and  $\sim 650$  atoms, respectively. In Fig. 1(b) the diameter has been transferred into the number of atoms with the aid of the formula  $n = (r/r_{WS})^3$ , where  $r$  is the cluster radius. The Wigner Seitz radius,  $r_{WS} = 0.203$  nm, was determined from the size of the rhombohedral unit cell for bismuth and the number of Bi atoms contained in the cell. It has to be noted that the detection efficiency of the TEM device decreases below diameters of 2 nm with a limit at about 1 to 1.5 nm. A fit of the distribution for sizes above 2 nm with the aid of a log-normal distribution (typical distribution for this type of aggregation sources) indicates that the maximum of the distribution occurs at smaller sizes containing about 80 atoms and that for sizes below  $n \sim 20$  only very low intensities are observed. The deposition of Bi clusters is made under soft landing conditions; i.e., the impact energy is of the order of 10 meV per atom (for  $n = 100$ ). A strong deformation due to the impact is therefore not probable, and we have assumed a spherical form. Strong deformation due to cluster surface interaction forces is believed to be small as well.

In very rare cases also large Bi clusters are observed, the structure of which is measured by TEM spectroscopy. In Fig. 1(c) a magnified image shows the internal structure of such a large cluster with a diameter of about 8 nm. Its crystalline structure shows rows of Bi atoms with a typical distance of  $0.36 \pm 0.05$  nm. This is slightly smaller than the expected bulk value.

### A. Mass/charge spectra and appearance sizes

In the following, collisions of 120 keV  $\text{Ar}^{8+}$  projectiles with neutral Bi nanoparticles in a size range of about  $\sim 2$  nm will be described. A typical mass/charge ( $n/q$ ) spectrum is shown in Fig. 2. As dominant contribution we observe the presence of small singly charged fragments with masses sizes between  $n = 1$  and  $n = 10$ . The peaks are rather wide, indicating that they are due to fragmentation processes. At larger  $n/q$  values, a wider distribution (magnified in intensity in Fig. 2 by a factor of 12) is observed which contains many peaks at noninteger numbers of  $n/q$ , thus demonstrating the presence of singly and multiply charged clusters with an intensity maximum at about  $n/q = 29$ .

In order to further analyze its structure we can zoom into the spectrum and show in Fig. 3 different  $n/q$  regions. Figure 3(a) displays the low  $n/q$  region, where only broad peaks of singly charged clusters of sizes  $n = 7$  and 8 are observed, which are due to fragmentation. The absence of very narrow peaks, which could be formed by single electron capture, indicates the absence of these sizes in the primary distribution. Figure 3(b) shows the presence of singly, doubly, and triply charged clusters. The doubly charged clusters  $\text{Bi}_{42}^{2+}$ ,  $\text{Bi}_{43}^{2+}$ , and  $\text{Bi}_{44}^{2+}$  are found to have a very narrow peak form. They overlap with the singly charged systems

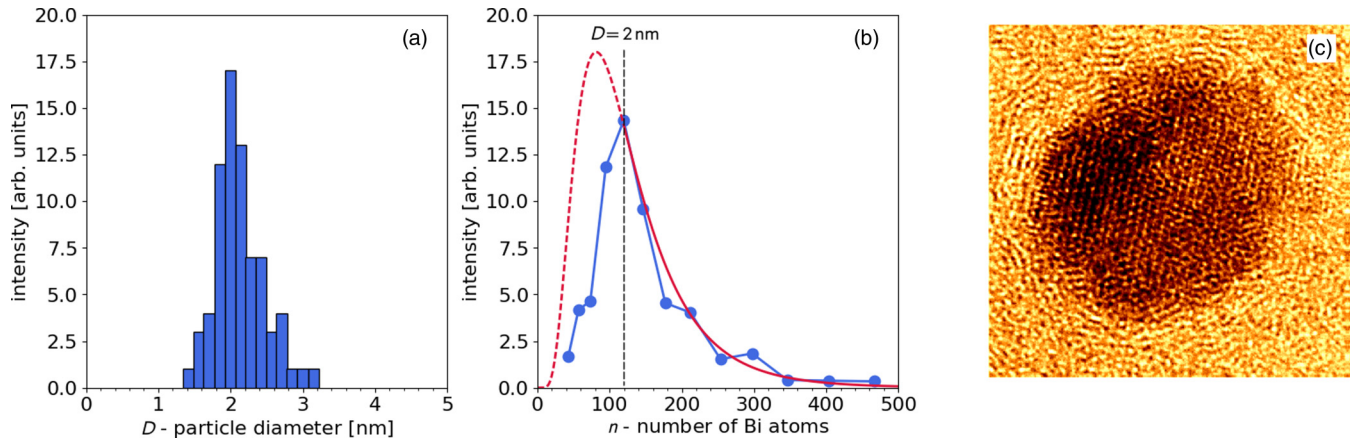


FIG. 1. (a) Histogram of the deposited cluster size distribution measured with a TEM microscope. (b) Size distribution as a function of the number of Bi atoms. Dots: experimental values, dashed curve: log-normal fit for the range above 120 atoms. (c) TEM image of a large Bi cluster with a diameter of about 8 nm.

$\text{Bi}_{21}^+$  and  $\text{Bi}_{22}^+$ , which are characterized by very broad peaks as to be seen by the broad base part of the peaks. The triply charged systems  $\text{Bi}_{63}^{3+}$ ,  $\text{Bi}_{64}^{3+}$ ,  $\text{Bi}_{65}^{3+}$ , and  $\text{Bi}_{66}^{3+}$  are found to be rather intense, which is probably due to the higher detection efficiency caused by the higher charge and hence the higher postacceleration before detection.  $\text{Bi}_{63}^{3+}$  and  $\text{Bi}_{66}^{3+}$  contribute as well to the intensity of the peaks for singly charged clusters  $\text{Bi}_{21}^+$  and  $\text{Bi}_{22}^+$ . In Figs. 3(c) and 3(d), we see that with increasing  $n/q$  values, cluster systems in higher charge states are observed; up to charge state  $q = 6$  they can be separated. In these regions the peaks are rather narrow and are likely due to pure multiple electron capture events.

By determining the intensity of mass and charge resolved clusters, one can construct mass spectra for a given charge state. These are shown in Fig. 4 for charge states  $q = 2$  to  $q = 4$ . In general the experimental spectra are characterized by a lower limit of the cluster size, then they pass through a maximum in intensity and loose intensity towards larger cluster sizes. In the large size regions, the analysis of the measured spectrum becomes difficult due to the limited mass

resolution of the spectrometer. Furthermore, the drop in intensity is partly caused by the decreasing detection efficiency for large clusters, in particular for clusters in low charge states. Therefore, the shape of the spectra does not agree with the log-normal distribution shown in Fig. 1(b) for neutral clusters.

The lower limit of the spectra reflects the stability of Bi clusters in different charge states. Metallic clusters can be described as a conducting sphere within the liquid drop model [16], which yields a low size limit for a given charge state. Based on ideas of Lord Rayleigh [19], large systems in low charges are stabilized with respect to fission processes (separation into two charged subsystems) by a fission barrier. This fission barrier decreases when the charge is increased or the size of the system is reduced. The stability of a charged system is described by the fissility parameter  $X$ , which is proportional to  $q^2/n$ . For the critical size at  $X = 1$ , the fission barrier disappears, and any spontaneous deformation of the system leads to charge-separating fragmentation (fission). This limit is predicted for cluster temperatures of  $T = 0$  K. Under these conditions the nanoparticles above this limit decay spontaneously upon infinitesimal small deformations, whereas those for which  $X$  is smaller than 1 are (meta)-stable.

As the cluster temperature in the experiment is higher than  $T = 0$  K, due to cluster formation ( $\sim 100$  K) and the collision process, a small finite barrier can be overcome. Furthermore, when the height of the fission barrier becomes equal to the activation energy for emitting neutral particles (evaporation), both processes occur in competition, thus, defining the so-called appearance size ( $n_{\text{app}}$ ). For large “hot systems,” de-excitation occurs via evaporation, thus reducing the cluster size and keeping the charge constant. When arriving at the appearance size  $n_{\text{app}}$ , charged fragments are emitted and lower sizes can no longer be observed in this charge state in the experimental spectrum. From Fig. 4 we can determine the appearance sizes, which are shown as red dots in Fig. 5. The values follow a straight line in a double-logarithmic representation, well below the critical sizes, corresponding to an  $X$  value of  $\sim 0.29$ . The dashed lines in Fig. 5 show the particle evolutions of hot clusters due to evaporation and fission. By the fission of clusters in a given charge state  $q$ , the intensity of the species in the next lower charge state

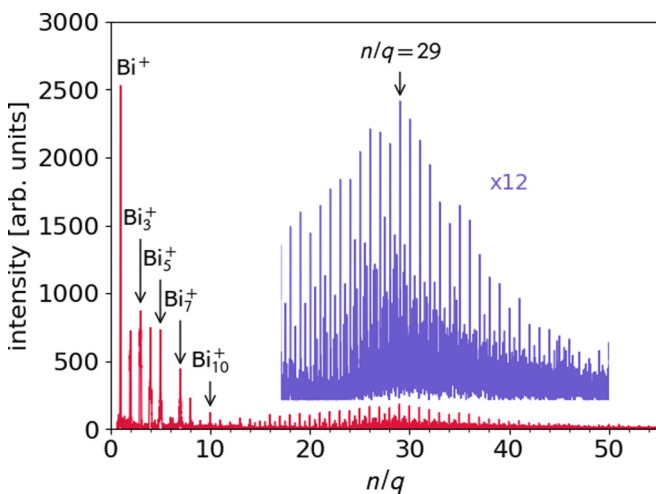


FIG. 2. Spectrum of Bi clusters (multi)-ionized and fragmented in collisions with  $\text{Ar}^{8+}$  ions at 120 keV.



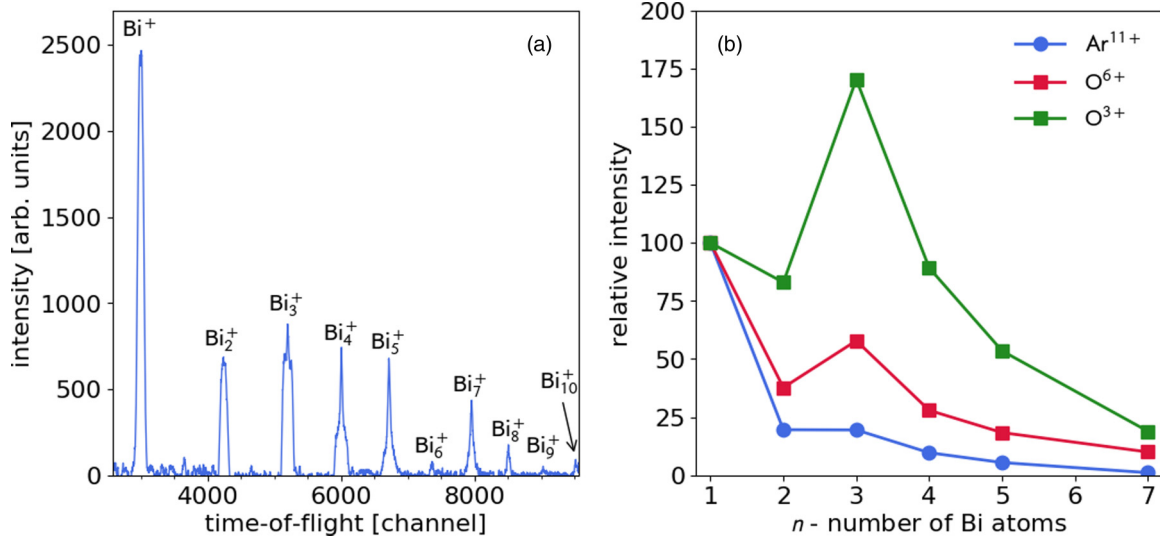


FIG. 6. (a) Intensity distribution of small size fragments produced in 120 keV  $\text{Ar}^{8+}$  collisions with neutral Bi clusters. (b) Variation of the cluster distribution for different projectiles: 45 keV  $\text{O}^{3+}$ , 90 keV  $\text{O}^{6+}$ , and 165 keV  $\text{Ar}^{11+}$ .

conclude that when Bi clusters are formed in higher charge states (higher  $X$  values), predominantly monomer ions are emitted in the fission process, whereas for lower charge states ( $X$  slightly above  $\sim 0.3$ ) the emission of trimers is becoming the most likely reaction channel. Similar results have been found for ion collisions with sodium clusters [20]. According to the observed peak width we identify these small clusters as being fragments produced with large kinetic energies, originating from different fragmentation pathways of larger clusters. For most of the peaks several processes with different kinetic energy releases contribute.

In Fig. 7(a) the peak form of the quadrumer  $\text{Bi}_4^+$  is shown in more detail, characterized by a large shoulder on each side. SIMION simulations [21] of the ion trajectories in the TOF spectrometer show that these correspond to fragments with kinetic energies of  $5.5 \pm 1.5$  eV [see Fig. 7(b)]. These high energetic ions are not well detected when they are emitted perpendicular to the extraction direction, and in consequence the corresponding distribution has a minimum at the central part. By subtracting the high-energy part from the total peak form, the distribution and the kinetic energy of the low-energy part can be estimated to be 0.28 eV [see Fig. 7(b)].

TABLE I. Critical sizes and appearance sizes for multiply charged  $\text{Bi}_n^{q+}$  clusters.

Charge	Bismuth		
	$n_{cr}$	$n_{app}^a$	$n_{app}^b$
2	6	$19 \pm 3$	5
3	14	$43 \pm 3$	38
4	24	$87 \pm 4$	
5	37	$121 \pm 4$	
6	53	$179 \pm 4$	

<sup>a</sup>Results obtained in collisions with  $\text{Ar}^{8+}$  ions.

<sup>b</sup>Results obtained by electron impact [10].

In Fig. 7(b) we show the kinetic energies for singly and doubly charged fragments in the  $n/q$  range from 1 to 18. Small singly charged fragments ( $n = 1-5$ , full blue circles) possess high kinetic energies of  $\sim 5$  eV decreasing towards larger sizes ( $n = 7$ ) to  $\sim 1$  eV. These fragments are attributed to fission of multiply charged Bi clusters. A more detailed discussion will follow in the next section describing coincidence measurements. In addition, a second group is observed (open blue circles) with lower kinetic energies approaching for larger sizes  $\sim 100$  meV. These species are also attributed to fragmentation or evaporation processes; however, the involved charge states are likely to be lower. For noninteger numbers of narrow peaks of doubly charged species [full red squares in Fig. 7(b)] which are above the appearance size of doubly charged clusters ( $n_{app} = 19$  and  $n/q = 9.5$ ) we observe doubly charged species with kinetic energies in the range of  $\sim 10$  meV. This means that initial clusters are ionized by double electron capture without further fragmentation. Narrow structures in the peaks with integer numbers in this range can also be attributed to doubly charged clusters [open red squares in Fig. 7(b)], in particular as their intensities are comparable with those of the noninteger clusters. Therefore, an estimation of possible contributions from singly charged clusters is difficult to make in this size range ( $n > 10$ ). However, their presence cannot be excluded.

### C. Coincident spectra

In the following we will discuss events where two charged fragments have been observed. As the particle detection efficiency is smaller than 1 ( $< 45\%$  depending on the mass and the kinetic energy of the fragments), the so-called “2STOP” spectra also contain contributions from events with higher multiplicities. In Fig. 8(a) we show a part of the 2STOP coincidence map, illustrating the time-of-flight of the second fragment (TOF2) as a function of the time-of-flight of the first one (TOF1).

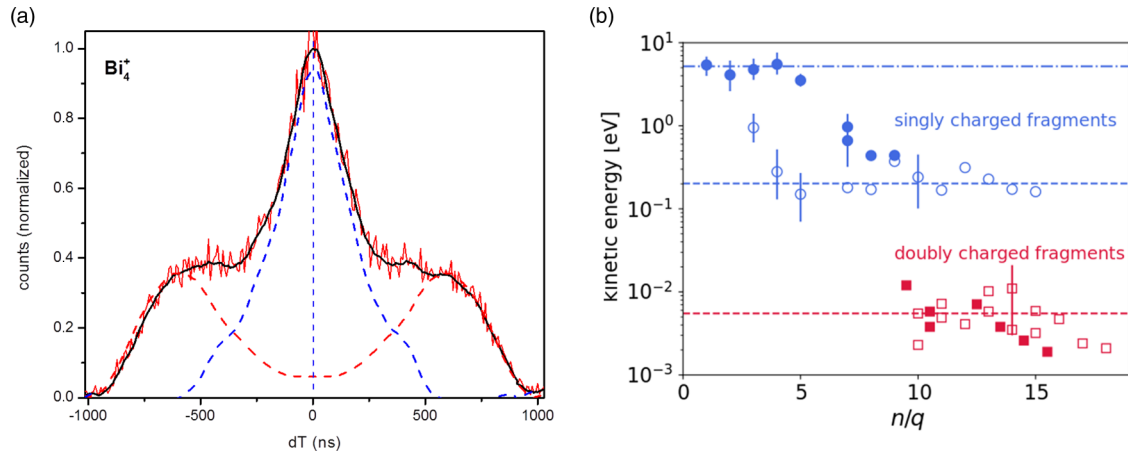


FIG. 7. (a) Experimental and simulated peak profiles of the singly charged  $\text{Bi}_4^+$  cluster. Full red curve: experimental data; black full curve: smoothed experimental data; dashed red curve (high-energy part): fitted data for  $\text{Bi}_4^+$  ions, isotropically emitted with kinetic energies of  $5.5 \pm 1.5$  eV; dashed blue curve (low-energy part): difference experimental data and fitted curve. (b) Kinetic energies of singly charged fragment ions (full and open blue circles) formed in collisions with  $\text{Ar}^{8+}$  projectiles and of doubly charged clusters (full and open red squares) formed by double electron capture.

TOF1 corresponds to a  $n/q$  range from 1 to 14, whereas the TOF2 axes spans an  $n/q$  range extending from 1 to about 290. One observes that the small fragments, in particular  $\text{Bi}^+$  and  $\text{Bi}_3^+$ , are measured in correlation with small, as well as with heavy, cluster residues. In Fig. 8(b) a zoom into the coincidence spectrum of  $\text{Bi}_3^+$  fragments is shown in more detail. Clearly so-called forward (at shorter TOF1 values) and backward lines (at longer TOF1 values) are observed. Furthermore, both lines separate more when the residue size (TOF2) is increased. This means that the maximum kinetic energy increases when the  $n/q$  value of the residue increases. From this we can conclude that clusters with larger  $n/q$  values are more highly charged producing  $\text{Bi}_3^+$  fragments with higher kinetic energies. To quantify this effect we performed horizontal projection through the bidimensional representation for specific  $n/q$  ranges. The resulting peak forms for  $\text{Bi}_3^+$  fragments are shown in Fig. 9 for correlations with different residue sizes, namely,  $n/q = 12$  and  $n/q = 93$ . Whereas in

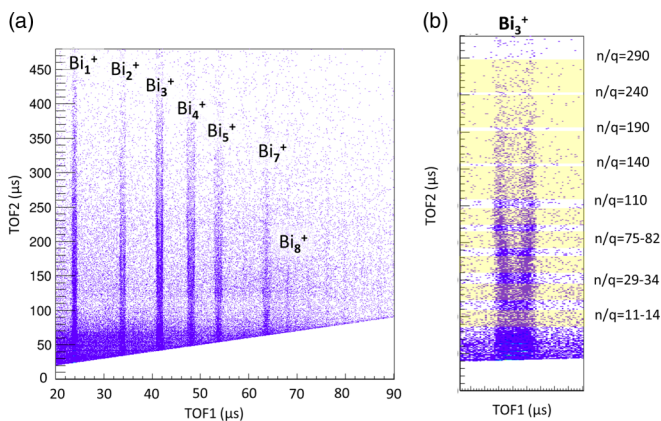


FIG. 8. (a) Part of the 2STOP coincidence map concentrating on correlations between small fragments and heavy residues. (b) Zoom into correlations of  $\text{Bi}_3^+$  fragments with heavy residues identified by their  $n/q$  values.

the first case we obtain a wider distribution without a stronger decrease in the central part, in the second case only a strong forward and a backward peak are observed. Thus, we attribute fragments correlated with small  $n/q$  values of the residue with the fragmentation of systems in low and high charge states, whereas in the case of higher  $n/q$  values mainly higher charge states are contributing.

In Fig. 10 we show the variation of the kinetic energy (high-energy part) as a function of the  $n/q$  value. For the trimer as well as for the monomer the energies increase with increasing  $n/q$  values. In the shown  $n/q$  range (10 to 290) the trimer energy increases from  $\sim 3$  to 5.3 eV, and the kinetic energies of the monomer are larger, increasing from 5.6 to 6.6 eV. This indicates that monomer ions are in general emitted from systems characterized by a higher fissility value  $X$ .

Kinetic fragment energies can be estimated by calculating the energetic position of the initial and final states based on the liquid drop model and applying different scenarios. For the trimer and  $n/q$  values below  $\sim 40$ , the measured kinetic energies can be reproduced with binary fission processes. As an example we might consider the fission of a cluster in charge state 7:

$$\text{Bi}_{200}^{7+}(n/q \sim 28; X \sim 0.35) \\ \rightarrow \text{Bi}_{197}^{6+}(n/q \sim 33; X \sim 0.25) + \text{Bi}_3^+(3.8 \text{ eV}).$$

The initial system is unstable with respect to fission as  $X > 0.29$ . After the emission of a trimer the residual system is characterized by an  $n/q$  value of 33 and a fissility of 0.25, which stabilizes the system in charge state 6. The kinetic energy of the fragment for this process is estimated within the liquid drop model by calculating the  $Q$  value [16] of the process to be 3.8 eV, which is close to the experimental value.

The high kinetic energies measured at  $n/q$  values above  $\sim 100$  require another scenario, namely, the decay of systems with  $X > 1$ . When calculating the energy surface of such systems, it is found that a large number of small-size fragments is emitted with energies in the 5 eV range, leaving the

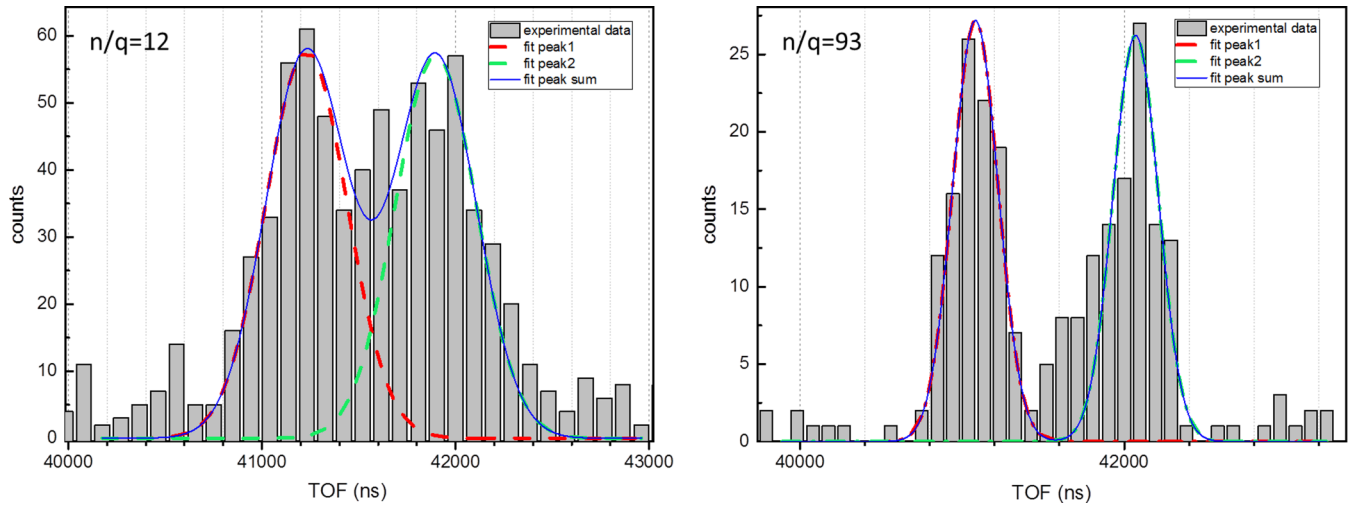


FIG. 9. Peak forms of the trimer ions measured in coincidence with residues with different  $n/q$  values. Left:  $n/q = 12$ , the spectrum does contain low-energy contributions from low charge state precursors. Right:  $n/q = 93$ , only high-energy fragments are observed.

residual system in a low charge state 1–3 [22,23]. Thus, a cluster  $\text{Bi}_{300}^{15+}$  can lead to final clusters in the  $n/q$  region of  $\sim 140$  after the emission of 13 small fragments. In the intermediate region of  $n/q$  values also sequential particles emission processes are expected to contribute to the measured spectra.

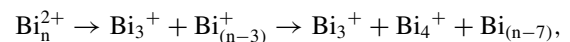
#### D. Coincident islands of small fragments

In Fig. 11 the coincidence islands for small fragments are shown. Before analyzing the island forms in more detail, we have to note that the sum of both fragment masses is below the mass of the decamer  $\text{Bi}_{10}^+$ . As these small clusters are not present in the primary beam, the fragmentation process always must include the emission of at least one third fragment, either neutral or charged. The momenta of those fragments, which are not detected, have to be taken into account, in particular when discussing the island's slope.

The shape of each island varies depending on the fragmentation dynamics and the superposition of different

fragmentation processes. Thus, very narrow shapes as well as signals in “butterfly” forms are observed. When comparing the correlation islands for the  $\text{Bi}_5^+$  fragments with those of different smaller fragments  $\text{Bi}_x^+$  (top row in Fig. 11), one observes that the distance of the subislands of forward and backward emission increases on the  $y$  axis ( $\text{Bi}_5^+$  fragment) when  $x$  is increased. This means that the average kinetic energy of  $\text{Bi}_5^+$  fragments increase with  $x$ . At the same time, the kinetic energy of  $\text{Bi}_x^+$  decreases. The general tendency corresponds to a binary decay; however, the energy ratios do not correspond to the mass ratio. Hence, a third body must be involved. In the following, we will discuss the coincidence islands ( $\text{Bi}_3^+$ ,  $\text{Bi}_4^+$ ) and ( $\text{Bi}^+$ ,  $\text{Bi}_2^+$ ) in more detail (both are shown in Fig. 12).

In the first case, different contributions are observed characterized by three lines with different slopes. The most intense part shows two maxima of forward and backward emission of both particles connected by a line with a slope of  $-0.55$ . This value shows that a third particle is involved in the decay process. This reaction can be explained by a two-step process, where in the first step charge separation of the assumed doubly charged parent ion occurs, and in the second step a neutral, nondetected fragment is emitted with low-energy release according to the following equation:



where  $n$  is the number of Bi atoms in the decaying system. When we assume that the energy release in the second evaporation step is small and that the velocities of both particles do not change, the initial size  $n$  can be calculated using the mass ratio for the second process and the measured slope value of  $-0.55$ . The result is  $\sim 11$ . The process where the  $\text{Bi}_4^+$  fragment is emitted first can be excluded as in that case a quite different slope value would be expected, namely,  $\sim -2.1$ . This result is plausible as the system  $\text{Bi}_{11}^{2+}$  is below the appearance size and, therefore, unstable with a fissility value of about  $X = 0.52$ .

The other two weaker contributions to the ( $\text{Bi}_3^+$ ,  $\text{Bi}_4^+$ ) island are characterized by a slope close to  $-1$  and  $+1$ . Whereas in the previous case the nondetected fragment was

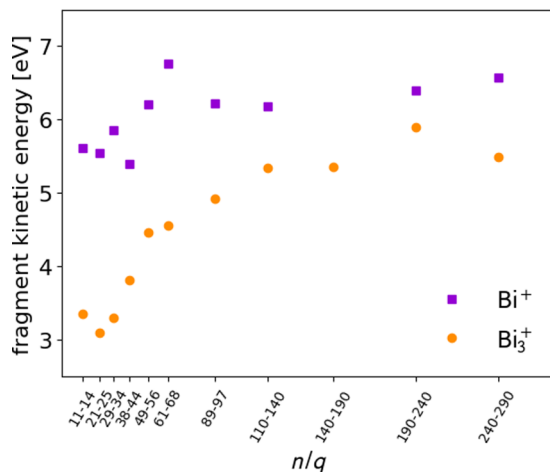


FIG. 10. Kinetic energies of monomer and trimer fragments, measured in coincidence with heavier fragments characterized by  $n/q = 11$  to 290.

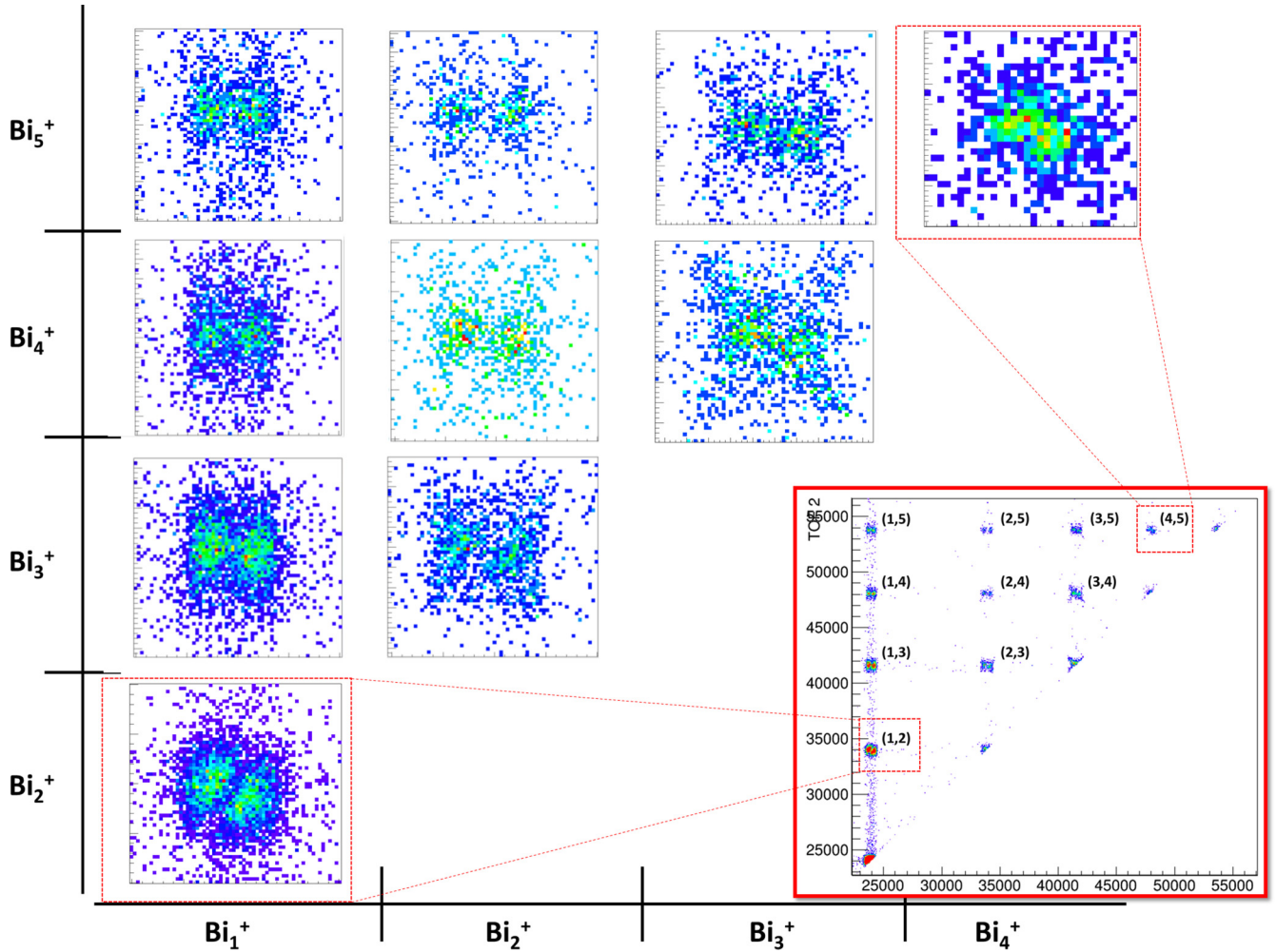
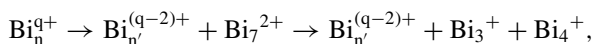


FIG. 11. Coincidence islands for small fragment pairs produced in  $\text{Ar}^{8+}$  collisions with  $\text{Bi}_n$  clusters.

emitted in the second fragmentation step, in these cases it is emitted during the first step according to the equation



where  $n'$  describes the size of the nondetected fragment. The slope of the fragmentation lines depends on the relative energy release in the first and the second fragmentation step. If the recoil momentum of the undetected particle is small compared to those of the  $\text{Bi}_3^+$  and  $\text{Bi}_4^+$  fragments one can expect a slope of  $-1$ . This is particularly true for  $q = 2$  and  $n = 7$  representing a binary fission [24,25]. However, the cluster with  $n = 7$  is very likely not present in the primary cluster distribution. On the other hand, when the recoil momentum in the first step is much larger than that occurring in the fragmentation of  $\text{Bi}_7^+$ , both fragments ( $\text{Bi}_3^+$  and  $\text{Bi}_4^+$ ) will be emitted in the same direction, yielding an overall slope of  $\sim +1$ . Comparable momenta will lead to signals more in the center of the map.

The island  $(\text{Bi}_1^+, \text{Bi}_2^+)$  is characterized by contributions with a average slope of  $\sim -0.71$ , which varies over a wide range of angles. By performing the same considerations as above, the decay of a doubly charged system would require a very small decaying system of size  $\sim 4$ , i.e., the evaporation

of a neutral atom and of the two detected fragments. Also these small clusters are not present in the primary cluster distribution. Furthermore, such a system would be characterized by a high  $X$  value of  $\sim 1.4$  inducing a spontaneous Coulomb explosion. Therefore, we propose that the observed decay is due to systems in higher charge states with high momenta involved. This means that they cannot be described in the present model discussed above.

#### IV. SUMMARY

We have analyzed the positively charged reaction products of  $\text{Ar}^{8+}$  collisions at 120 keV with neutral Bi clusters containing between  $\sim 10$ – $20$  and a few hundreds of atoms (up to 650). The spectra for individual charge states up to  $q = 6$  and the corresponding appearance sizes have been determined showing good agreement with the liquid drop model. The intense distribution of small-size fragments is found to be produced by multiple electron capture into unstable cluster states followed by fission processes. From the analysis of the kinetic energy of the fragments it is concluded that small fragments ( $n = 1$  to 5) do have a high-energy component of the order of 5 eV, which stems from the fission of clusters in higher charge states. Measurements performed

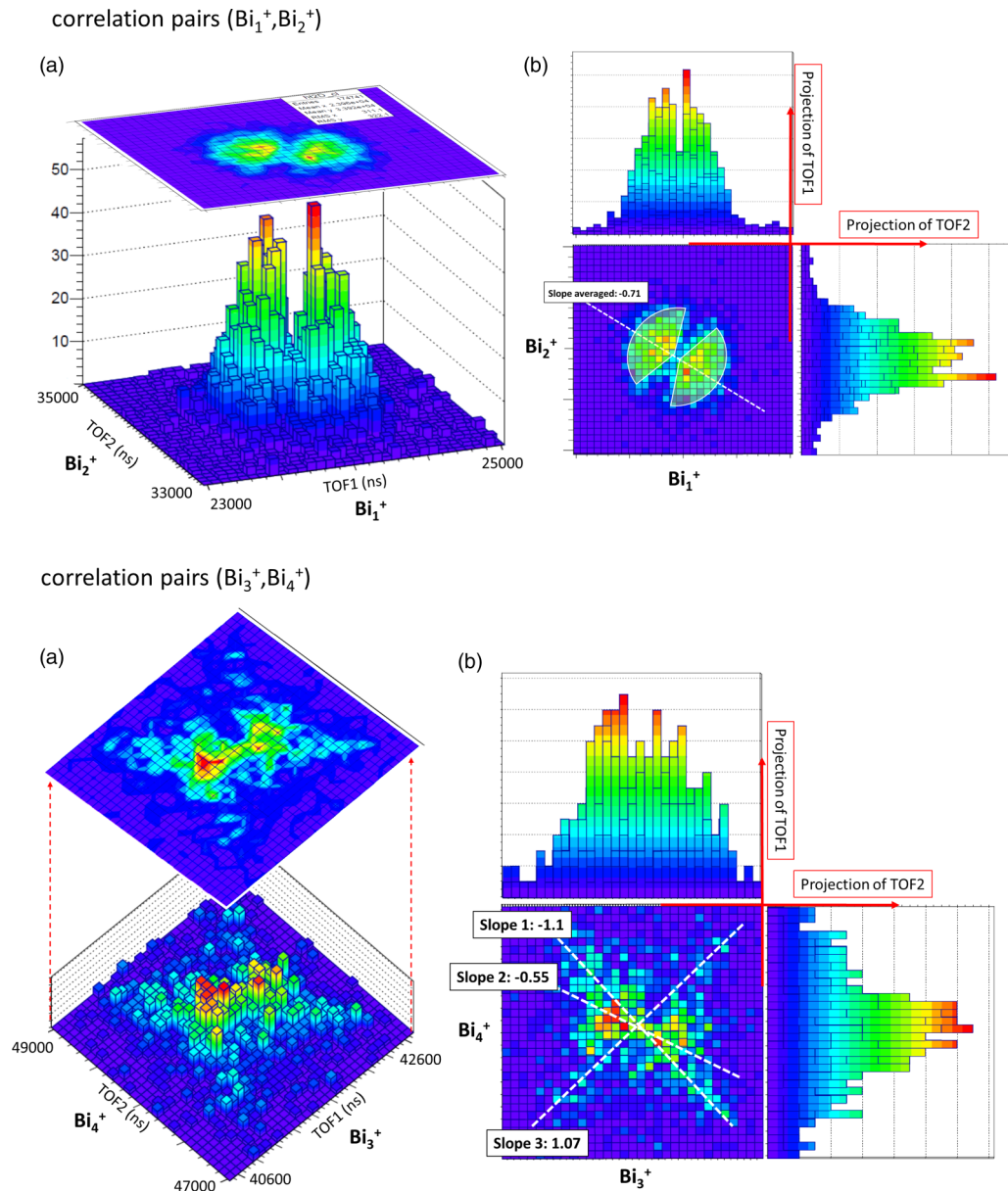


FIG. 12. Different presentations of the islands of the correlation pairs ( $\text{Bi}_1^+, \text{Bi}_2^+$ ) (upper part) and ( $\text{Bi}_3^+, \text{Bi}_4^+$ ) (lower part). The given lines indicate the slopes of different processes.

in coincidence with larger residues yield information on the underlying fragmentation mechanisms, as binary fission for systems with  $n/q < 40$  and simultaneous or sequential emission of several small fragments for larger  $n/q$  values. The coincident analysis between small fragments ( $n < 5$ ) shows that “third” nondetected particles participate in the decay process and demonstrates that both detected fragments can be emitted in two-step processes in the same or in the opposite direction.

#### ACKNOWLEDGMENTS

The research was conducted at the CIMAP laboratory on the site of GANIL in Caen, France. We thank Jean-Marc

Ramillon, Claire Feierstein-Plancq, and Thierry Been for technical development of a magnetron source and technical assistance and Isabelle Monnet and Jean-Gabriel Mattei for recording of AFM and TEM images. A.M. was funded by the European Union Seventh Framework Programme (PEOPLE2013-ITN-ARGENT project 2014-2017) under Grant No. 608163. We furthermore acknowledge the support received from INCa-ITMO (Grant No. PC201307, BIOHYDRA project) within the Programme Plan Cancer 2009-2013 (Inserm), the COST actions NANO-IBCT (Nanoscale insights into Ion Beam Cancer Therapy, MP1002), and XLIC (XUV/X-ray light and fast ions for ultrafast chemistry, CM1204).

- [1] J. Conde, G. Doria, and P. Baptista, *J. Drug Deliv.* **2012**, 751075 (2012).
- [2] E. Porcel, S. Liehn, H. Remita, K. K. N. Usami, Y. Furusawa, C. L. Sech, and S. Lacombe, *Nanotechnology* **21**, 085103 (2010).
- [3] Z. Kuncic and S. Lacombe, *Phys. Med. Biol.* **63**, 02TR01 (2018).
- [4] A. Solov'yov, *Nanoscale Insights into Ion-Beam Cancer Therapy* (Springer, Heidelberg, 2017).
- [5] C. Sicard-Roselli, E. Brun, M. Gilles, G. Baldacchino, C. Kelsey, H. McQuaid, C. Polin, N. Wardlow, and F. Currell, *Small* **10**, 3338 (2014).
- [6] M. Hossain and M. Su, *J. Phys. Chem. C* **116**, 23047 (2012).
- [7] C. A. Hoffman, J. R. Meyer, F. J. Bartoli, A. Di Venere, X. J. Yi, C. L. Hou, H. C. Wang, J. B. Ketterson, and G. K. Wong, *Phys. Rev. B* **48**, 11431 (1993).
- [8] Y. Luo, C. Wang, Y. Qiao, M. Hossain, L. Ma, and M. Su, *J. Mater. Sci.: Mater. Med.* **23**, 2563 (2012).
- [9] T. M. Bernhardt, B. Kaiser, and K. Rademann, *Z. Phys. D* **40**, 327 (1997).
- [10] W. Schulze, B. Winter, and I. Goldenfeld, *Phys. Rev. B* **38**, 12937 (1988).
- [11] R. Kelting, U. S. A. Baldes, T. Rapp, D. Schooss, P. Weis, C. N. F. Weigend, and M. M. Kappes, *J. Chem. Phys.* **136**, 154309 (2012).
- [12] M.-H. Mikkela, M. Tchapyguine, S. Urpelainen, K. Jankala, O. Björneholm, and M. Huttula, *J. App. Phys.* **112**, 084326 (2012).
- [13] C. Bréchnignac and P. Cahuzac, *Chem. Phys. Lett.* **117**, 365 (1985).
- [14] M. Koskinen and M. Manninen, *Phys. Rev. B* **54**, 14796 (1996).
- [15] F. Chandezon, C. Guet, B. A. Huber, D. Jalabert, M. Maurel, E. Monnard, C. Ristori, and J. C. Rocco, *Phys. Rev. Lett.* **74**, 3784 (1995).
- [16] U. Näher, S. Björnholm, S. Frauendorf, F. Garcias, and C. Guet, *Phys. Rep.* **285**, 245 (1997).
- [17] T. Bergen, X. Biquard, A. Brenac, F. Chandezon, B. A. Huber, D. Jalabert, H. Lebius, M. Maurel, E. Monnard, J. Opitz, A. Pesnelle, B. Pras, C. Ristor, and J. C. Rocco, *Rev. Sci. Instrum.* **70**, 3244 (1999).
- [18] Y. Huttel (ed.), *Gas-Phase Synthesis of Nanoparticles* (Wiley-VCH, Verlag GmbH & Co. KGaA, Singapore, 2017).
- [19] F. R. S. Rayleigh, *Philos. Mag.* **14**, 184 (1882).
- [20] C. Guet, X. Biquard, P. Blaise, S. A. Blundell, M. Gross, B. A. Huber, D. Jalabert, M. Maurel, L. Plagne, and J. C. Rocco, *Z. Phys. D* **40**, 317 (1997).
- [21] SIMION: Ion and Electron Optics Simulator, version 8.1, developed by Scientific Instrument Services, Inc. (SIS).
- [22] G. E. Ntamack, B. A. Huber, F. Chandezon, M. G. K. Njock, and C. Guet, *J. Phys. B* **35**, 2729 (2002).
- [23] P. Blaise, S. A. Blundell, C. Guet, and R. R. Zope, *Phys. Rev. Lett.* **87**, 063401 (2001).
- [24] K. Schäfer, W. Baek, K. Förster, D. Gassen, and W. Neuwirth, *Z. Phys. D: At. Mol. Clusters* **21**, 137 (1991).
- [25] S. Bari, P. Sobocinski, J. Postma, F. Alvarado, R. Hoekstra, V. Bernigaud, B. Manil, J. Rangama, B. Huber, and T. Schlathöler, *J. Chem. Phys.* **128**, 074306 (2008).